

Optoacoustic imaging system with improved collection efficiency.

Dmitri Tsyboulski^a, André Conjusteau^a, Sergey A. Ermilov^a, Hans-Peter F. Brecht^a, Anton Liopo^a,
Richard Su^a, Vyacheslav Nadvoretzky^a, Alexander A. Oraevsky^{a*}

^a TomoWave Laboratories, Inc., 675 Bering Drive, Suite 575, Houston, TX, USA 77057-1203

ABSTRACT

We introduce a novel experimental design for non-invasive scanning optoacoustic microscopy that utilizes a parabolic surface for ultrasound focusing. We demonstrate that off-axis parabolic mirrors made of sufficiently high acoustic impedance materials work as ideal reflectors in a wide range of apertures and provide lossless conversion of a spherical acoustic wavefront into a plane wave. We further test the performance of a custom optoacoustic imaging setup which was developed and built based on these principles. The achieved resolution limit of 0.3 mm, with NA of 0.5 and the transducer bandwidth of 5 MHz, matches the resolution limit defined by diffraction. Although further improvements of current experimental setup are required to achieve resolution similar to leading microscopy systems, this proof-of-concept work demonstrates the viability of the proposed design for optoacoustic microscopy applications.

Keywords: optoacoustic microscopy, photoacoustic microscopy, ultrasound imaging, high resolution, off-axis parabolic mirror, ultrasound focusing

1. INTRODUCTION

Optoacoustic or photoacoustic imaging is a new technology that allows non-invasive and high-resolution imaging of internal organs and blood vasculature in small animals and humans. Ultrasound generated as a result of laser pulse absorption propagates throughout tissues virtually without any distortions at large distances and can be detected by specialized transducers or transducer arrays. Using the measured transient acoustic profiles, a tomographic image of initial pressure distribution can be reconstructed. Since the contrast in such image is directly related to the sample absorptivity, this methodology allows to perform functional imaging and non-invasive measurement of a number of physiological parameters [1-3]. Optoacoustic microscopy is a high-resolution variant of optoacoustic imaging technology utilizing significantly higher ultrasound frequencies and numerical apertures (NA) to generate *in vivo* images with resolution below 50 μm at depths of several millimeters. Several optoacoustic microscopy systems that utilize different strategies to focus ultrasound were developed over the recent years [4-9]. The most basic designs rely on a focused transducers to perform scanning microscopy imaging [9, 10]. Unfortunately, due to technological challenges in manufacturing high-quality focused piezoelectric elements, their apertures are typically limited to 0.1 - 0.25, which, in its turn, limits the resolution of these systems. Costly annular arrays are useful for extending depth of field of optoacoustic imaging, but they can not achieve diffraction-limited focusing with a limited number of elements [11].

Several unique optoacoustic microscopy systems that achieved unprecedented resolution and imaging depths with focused ultrasound have been developed over the recent years. Maslov, *et al.*, introduced an experimental design that utilizes a concave fused silica lens with NA of 0.44 for ultrasound focusing coupled to a flat transducer operating at high central frequencies of 50 MHz and above [3]. Since the direct sample illumination path is blocked by a transducer, the light is directed at oblique angles by a custom-designed annular dark-field illuminator. With this design, high resolution imaging at depths up to 3 mm in test samples and up to 1 mm in live tissues was demonstrated [10]. The dark-field photoacoustic microscope utilizes high-frequency and ultra-sensitive resonant transducers for ultrasound detection to achieve high resolution. However, strong acoustic attenuation at high frequencies is likely to severely limit its imaging depth. Focusing ultrasound with refractive elements made of high acoustic impedance materials presents a number of challenges. It is hardly possible to achieve perfect conversion of a spherical wavefront into a plane wave without incurring significant losses of the signal. Besides reflections, significant losses arise due to the conversion of longitudinal acoustic waves into shear waves at the water-quartz interface. It is possible to reduce reflective losses by introducing a $\lambda/4$ anti-reflection coating, however, only at the expense of further limiting the detection bandwidth of the acoustic system. Insertion losses of $\sim 90\%$ at resonance and more than 99% off-resonance are typical for such focusing elements [11].

* AAO@tomowave.com, phone 1 713 212-7550; fax 1 713 212-7597; www.tomowave.com

The most recent and most advanced optoacoustic microscopy setup that set a new record in high-resolution ultrasound imaging was developed by Zhang, *et al.* [5, 6]. This setup utilizes a custom Fabry-Perot interferometric planar sensor that consists of a thin polymeric film sandwiched between short-pass dielectric mirrors to detect incoming pressure waves. The sample is excited by laser pulses through an optically transparent region of the sensor. Projections of transient pressure profiles on the sensor plane are recorded by scanning its surface with a focused probe laser beam to measure the dynamics of localized changes in film thickness as ultrasound propagates through the sensor. After point by point scanning of the whole sensor area the image is reconstructed to reveal internal structures in great details. Major benefits of this design include most efficient straight downward light delivery, close proximity of the sensor to the area of interest, exceptionally small insertion losses, broadband detection in a wide range of frequencies up to 40 MHz, and high numerical aperture. With this design, the developer team set new records in non-invasive optoacoustic microscopy by demonstrating high-resolution images at depths of 3 and 5 mm measured in mouse brain and soft tissues, respectively [6, 12]. Sensitivity level for the interferometric sensor on the order of ~200 Pa for 20 MHz bandwidth was reported [5]. Although it may be found disputable, we believe that broadband piezoelectric transducers of sufficiently large size may provide better sensitivity. Thus, a scanning microscopy setup that utilizes a single-detector element may potentially detect acoustic signals coming from deeper layers of tissues under the conditions of most effective light delivery and absence of insertion losses as achieved in the interferometric optoacoustic microscope.

In this report, we introduce a novel experimental design that will potentially allow us to achieve diffraction-limited ultrasound focusing. Here we discuss the feasibility of using off-axis parabolic reflectors for optoacoustic microscopy applications, which, to our best knowledge, have not been attempted previously. Parabolic mirror will perform an ideal and lossless conversion of a spherical wavefront into a plane wave to allow the use of any flat-surface transducer of sufficient size for ultrasound detection. This type of reflectors may provide exceptionally large NA values, up to 0.7. It is expected, that improved collection efficiency of the experimental system will permit us to achieve the desired resolution limit at lower frequencies and, consequently, extend the imaging depth limit even further.

2. PRINCIPLES OF EXPERIMENTAL DESIGN

The resolution of an imaging system is defined by its collection efficiency and the wavelength that is used for imaging. Given the wave nature of ultrasound, one may estimate the diffraction-limited lateral resolution R_L using standard optical equation that describes full width at half maximum (FWHM) of a Gaussian point spread function of a focused light:

$$R_L \approx 0.5 \frac{c}{\Delta f \cdot NA} \quad (1)$$

where $c \approx 1500$ m/s is the speed of ultrasound in water, Δf is the frequency bandwidth of a detection system, and NA defines the numerical aperture of the system. Since ultrasound detection is time-resolved with typical sampling rates in the range of 0.1 – 1 GHz, the axial resolution, in fact, is significantly better than lateral and is defined by the transducer impulse response characteristics. For example, one may estimate that a resolution of ~50 μm is attainable with NA of 0.7 and bandwidth of 20 MHz. It should be noted, that the resolution limit R_L from eq. 1 is only an approximate value given that optoacoustic signals are typically non-Gaussian, bipolar, and their detected frequency spectrum is subject to distortions due to limited detection bandwidth, frequency dependent acoustic attenuation, and interference of positive and negative wavefronts. However, the general principles remain the same: one must either decrease the wavelength or increase NA of the system to achieve better resolution.

By definition, a parabola is the family of points equidistant from a focal point (focus) and a line (directrix). In Descartes coordinates, the parabola is described by a function $y(x,a)=x^2/4a$, where a is the distance between the parabola vertex and a focal point. It follows from the definition that the incoming flat wavefront will be focused by a reflecting parabolic surface to a focal point. Off-axis parabolic mirrors found their use in optics for light collimation and focusing. Current level of technology allows relatively inexpensive production of parabolic mirrors with arbitrary shape and micrometer-scale accuracy. Although this level of precision is not adequate for optical microscopy applications, it exceeds the requirements needed for ultrasound focusing by more than an order of magnitude. Using the definition of a parabola one may easily calculate geometrical numerical aperture of an off-axis parabolic reflector. Thus, for a set of parameters a , z , and F , where z and F represent an elevation relative to a focus and a working distance respectively (also see Fig. 1a), NA is given as:

$$\sin \alpha = \frac{a - F^2/4a}{a + F^2/4a} \quad \sin \beta = \frac{z}{z + 2a} \quad NA(a, z, F) = \sin\left(\frac{\alpha + \beta}{2}\right) \quad (2)$$

Fig. 1b shows NA as a function of a -parameter at realistic z and F values. The red solid lines in Fig. 1 correspond to the actual parabolic mirror in this work. The minimum distance sound has to travel until it reaches a transducer equals $z+2a$. Since the selection of high a and z values for reflector design is impractical due to acoustic attenuation at large distances, the acceptable range of travel from the source to a transducer is $\sim 3 - 4$ cm. Clearly, off-axis parabolic reflectors can provide large collection efficiency with NA values reaching 0.6 – 0.7 (see Fig. 1b). To achieve complete reflection of ultrasound from a surface, the angle of incidence must exceed the critical angle for both refracted longitudinal (lw) and shear wave (sw) components in the material of a reflector. Table 1 summarizes the speed of sound for both types of ultrasound waves in selected materials, as well as critical angles at the water/material interface. Fig. 1c shows variation of the angle of incidence for a parabolic curves with different a values, as well as sw critical angle cut-offs for these materials. As follows from Fig. 1c, the aperture α is limited by the magnitude of shear wave critical angle of the reflector surface. Limitations for β arise from the requirement to minimize traveling distance from the ultrasound source to the detector.

Table 1. Physical properties of selected materials and critical angles at water/material interface [13].

Material	sw velocity, mm/ μ s	lw velocity, mm/ μ s	sw critical angle [#] , °	lw critical angle [#] , °
rolled aluminum	3.04	6.42	29.6	13.9
crown glass	2.8	5.1	32.4	17.1
fused silica	3.75	5.7	23.6	15.3

[#] - assuming speed of sound in water at 36 °C, which is 1540 m/s

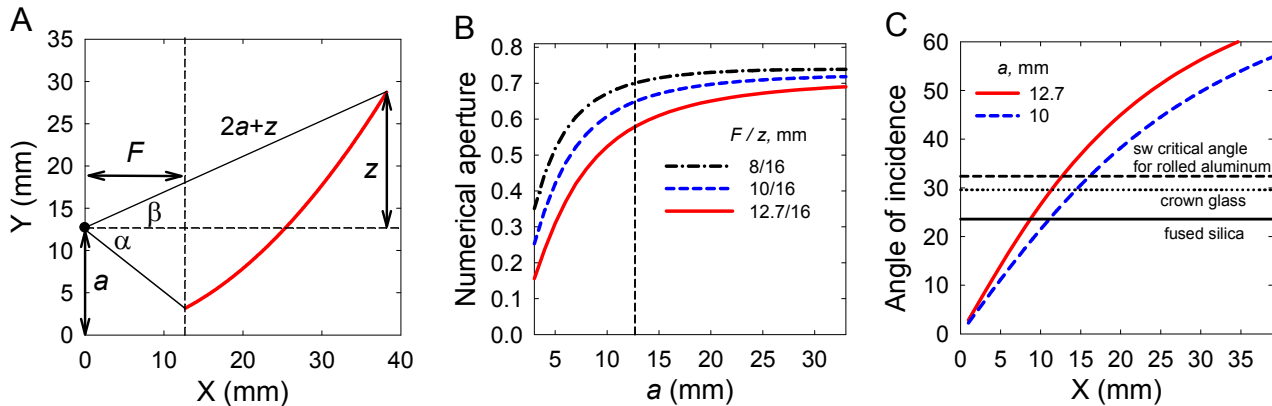


Fig. 1 (A) Cross-section of a parabolic mirror defined by parameters $a=F=12.7$, and $z=16$ mm. (B) Numerical aperture of a parabolic reflectors as a function of coefficient a and selected F and z values. Vertical dashed line is plotted at $a=12.7$ mm. (C) Variation in the angle of incidence at the surface of parabola's as a function of X-coordinate. Two parabolic surfaces with different a values are shown.

Ultrasound attenuation in tissues primarily results from scattering and by far exceeds viscous friction losses in water. For comparison, the frequency-dependent acoustic attenuation coefficient in water equals $2.17 \cdot 10^{-15} \times f^2$ dB/cm/MHz² [14], while in tissues it appears typically in the range between $0.3 - 0.7 \times f$ dB/cm/MHz [15, 16]. As shown in Fig. 2, the losses of ultrasound in water are significantly smaller as compared to losses in biological tissues. Therefore, the distance between the source and a transducer on the order of several centimeters is acceptable for imaging applications.

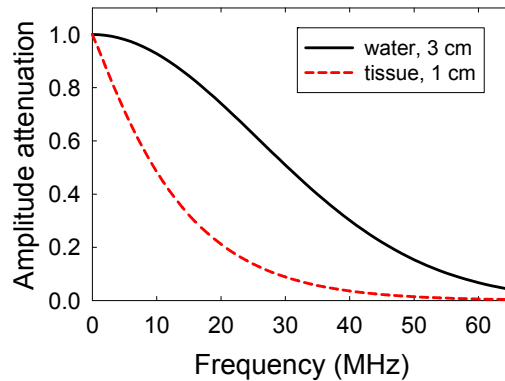


Figure 2. Frequency-dependent ultrasound attenuation in water and biological tissues at the distance of 3 and 1 cm, respectively.

3. EXPERIMENTAL SETUP

We have created our experimental setup on the base of a previously described small animal optoacoustic imaging system (Seno Medical Devices, San Antonio, TX) [9]. The system utilizes a pulsed Nd-YAG +Ti:Sa laser (Quanta System SPA, Olona, Italy) operating at 775 nm. Laser pulses with duration of less than 10 ns, adjustable energy level between 0 and 10 mJ, and a pulse repetition rate of 10 Hz are delivered via optical fiber to the sample. The fiber output is refocused with a lens on the sample surface to a spot of ~ 5 mm in diameter. Focusing of ultrasound was achieved with a 90° off-axis parabolic mirror (Edmund Optics, parent focal length - 12.7 mm, reflected effective focal length and Y offset - 25.4 mm). To allow direct illumination, a 5 mm hole was drilled through the mirror. We estimate that only $\sim 5\%$ of the mirror surface was affected. A custom transducer 25.4 mm in diameter was manufactured by sandwiching 28 μm thick polyvinylidene fluoride (PVDF) metallized film between thin copper electrodes and mounting it on an acrylic backing. The transducer was mounted in front of the mirror on a tilt stage to allow elevation and longitude adjustments. The assembly is mounted on a motorized XYZ stage and submerged in a water tank to allow 3D scanning of the samples. The optoacoustic signal is amplified by 17 dB (SEA A17dB Hydrophone Preamplifier 17 dB, 0.005 – 25 MHz) and digitized by a 12-bit analog-to-digital converter with a sampling rate of 104 MHz.

4. EXPERIMENTAL RESULTS AND DISCUSSION

The impulse response characteristics of the transducer were determined with custom-made plane wave Δ -source, described elsewhere [17]. The transducer impulse response and its frequency spectrum are shown in Fig. 4. The FWHM of the peak in Fig. 4 equals ~ 60 ns. Its frequency spectrum shows 4.9 MHz bandwidth at -6dB, which is significantly lower than expected for 28 μm thick PVDF film. We note, that transducers of a smaller size, e.g. 5 mm in diameter made in a similar fashion typically exhibit frequency bandwidths of 15-20 MHz. In the impulse response, we observe a sharp rise to the maximum followed by a significantly slower fall off. This fast increase has a characteristic timescale similar to a Gaussian with full width at half maximum (FWHM) of 30 ns, corresponding to ~ 15 MHz bandwidth. The reduced

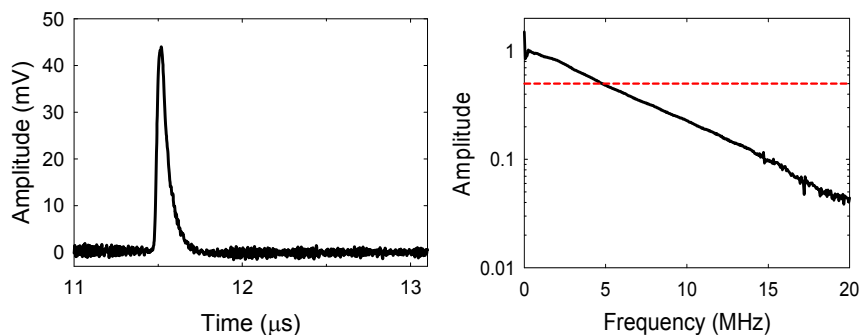


Figure 4. Impulse response of the custom transducer and its frequency spectrum. The sign of the pulse is inverted for clarity.

bandwidth of a large transducer is likely a result of two effects: one being the non-uniformity our Δ -source wavefront over the large area of a transducer, and the second being imperfections in transducer manufacturing which result in a non-ideal flatness of the piezoelectric film. Thus, the measured transducer bandwidth should not be considered as true bandwidth, but rather a lower bandwidth limit.

After tedious alignment, we performed a series of test scans to assess the resolution of the system. As a spherical wave source we selected a steel ball bearing with diameter of 0.78 mm. The ball bearing was painted with a permanent black-ink marker and mounted on a Rexolite support. Fig. 5 shows the maximum intensity projection (MIP) volumetric image of the ball, as well as 2D cross-sections at the center of this image. A Gaussian fit yields FWHM parameters of 0.36 ± 0.03 and 0.36 ± 0.02 mm for X and Y directions, respectively. The impulse response of the system at the maximum signal intensity and its frequency spectrum are shown in Fig. 5b,c. The rise in the impulse response is ~ 50 ns, which is slower than the rise in the transducer response to plane wave Δ -source, yet the width of the peak is slightly smaller and equals ~ 44 ns. It is remarkable that a spherical wavefront is converted to a nearly ideal plane wave over such a large area virtually without distortions. Fast Fourier transform (FFT) shows that the -6 dB cutoff lies between 1 – 10.5 MHz, The FFT profile shows symptoms of pulse differentiation, similar to those observed in electric circuits with a low impedance load. However, in the present case it is not related to electronics, but rather is a result of interference from the backward-propagating negative and forward-propagating positive wavefront reflected from the steel surface.

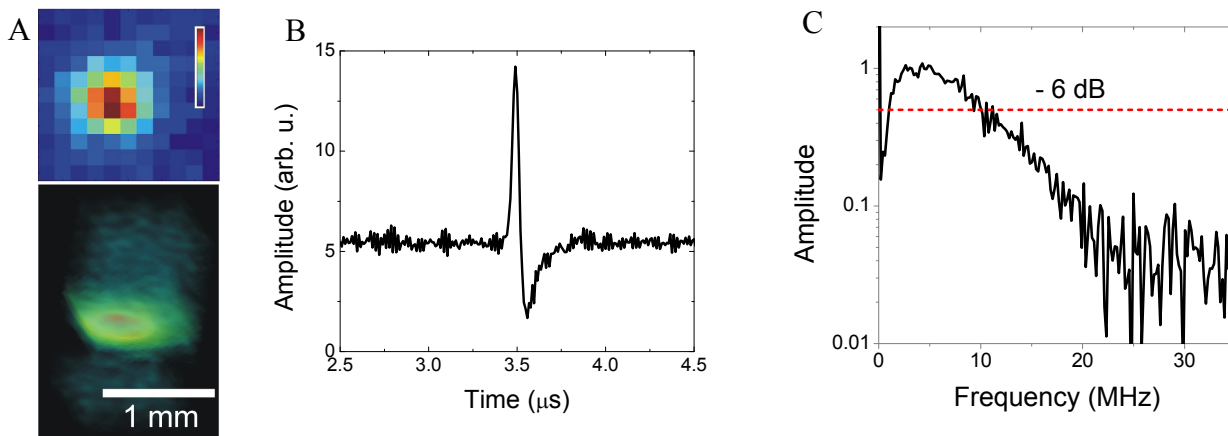


Fig. 5. (A) Cross-section and volumetric MIP images of a painted 0.78 mm steel ball bearing. The scanned area is 1.1×1.1 mm. (B) Transducer impulse response at the maximum of optoacoustic signal intensity. The sign of the pulse is inverted for clarity. (C) FFT profile of a transducer impulse response.

Next, we imaged a phantom made of crossed human hairs having a diameter less than $100 \mu\text{m}$. The corresponding MIP optoacoustic image is shown at Fig. 6a. To assess spatial resolution, we extracted linear intensity profiles across the hairs at the point of maximum signal intensity. Gaussian fits yield FWHM values of 0.29 and 0.33 mm. The impulse response

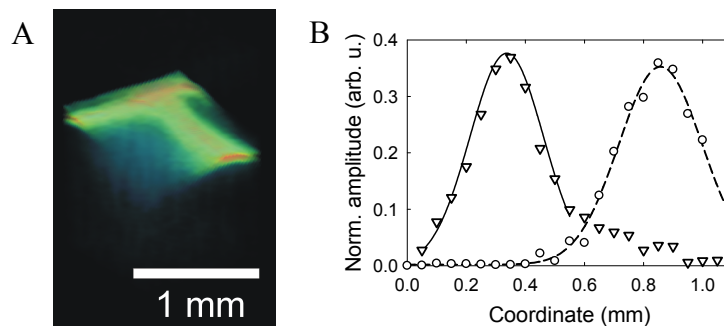


Fig. 6. (A) Volumetric MIP image of a pair of crossed hairs. (B) Intensity profiles across both hairs measured at the position of maximum intensity.

at the position of maximum intensity and its frequency spectrum are shown in Fig.7. Notably, the limit of 0.3 mm corresponds to the resolution limit of an imaging system with frequency bandwidth of 5 MHz and NA of 0.5. From the impulse response we measure approximately 50 ns FWHM peak width, and a bandwidth of 5.2 MHz.

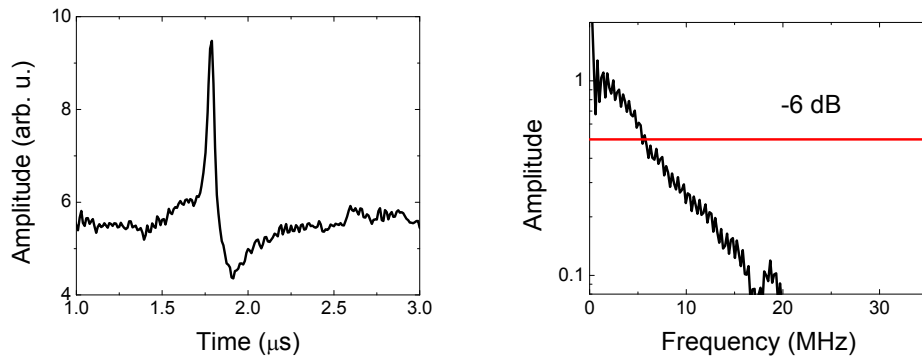


Figure 7. Transducer impulse response at the maximum of optoacoustic signal intensity and its FFT spectrum.

As in the plane-wave Δ -source, a uniformly irradiated and sufficiently thin absorbing layer should produce a spherical wavefront with Gaussian pressure profile along a radial direction. Although the recorded impulse responses (Fig. 5b and Fig. 7) have sharp features on the timescale of ~ 50 ns, they exhibit non-Gaussian and bipolar character. It is important to characterize the pressure profile reflected from a parabolic mirror to assess its uniformity, reveal potential distortions,

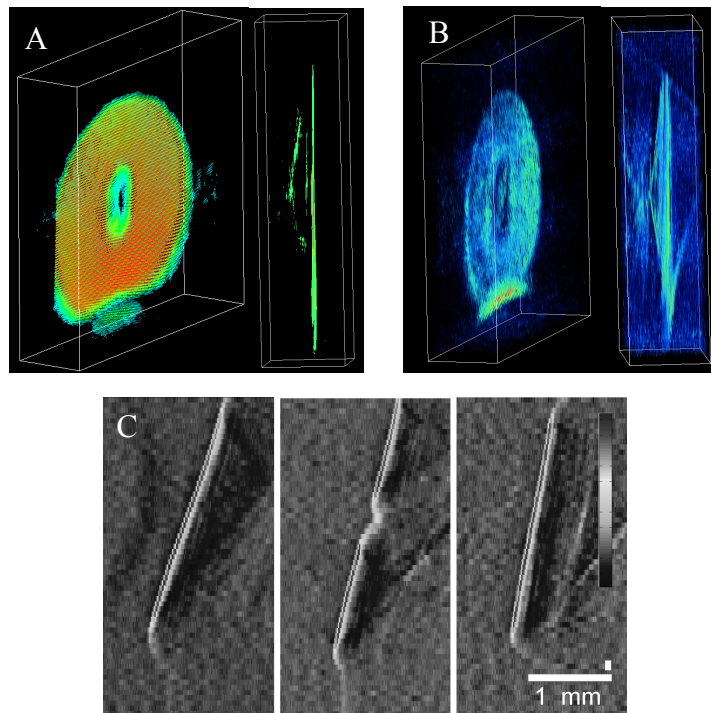


Figure 8. (A) Negative and (B) positive pressure MIP images of the planar wavefront recorded by scanning its cross-section with a small-size transducer. The dimensions of the enclosing frame are $30.5 \times 30.5 \times 7.3$ mm. (C) Horizontal wavefront cross-sections. The size of scale bars in horizontal and vertical dimension is 1 mm.

and understand their influence on the imaging resolution of the experimental setup. In place of a large transducer, we position a broadband hydrophone (Onda, GL-0200) with a small-size piezoelectric element of 200 μm in diameter. The hydrophone was mounted on a XY stage in front of the reflector. Given a small size and a relatively large acceptance

angle, more than 5° for frequencies below 20 MHz [17], the transducer will allow point by point measurements of the reflected ultrasound wave. Figure 8 shows the MIP images of a measured pressure wavefront and its XY cross-sections at different Z positions. For clarity, negative and positive signals are plotted independently at Fig. 8a and b. The negative wavefront is remarkably flat across the whole reflector area except diffraction effects at the edges and a hole in the center of a reflector. As seen from cross-sectional images, the diffraction at the edges of the mirror erodes only a small portion of a wavefront at 0.5-1 mm distance from the edge of the reflector, approximately 5-6% of the total wavefront area. The wavefront, however, is slightly warped, as shown at Fig. 8c. Note that the horizontal scale is greatly expanded in these images to reveal such warping. Wavefront deformation is likely to result from an imperfect alignment of a spherical wave source and a focal point of a reflector in this experiment. The maximum angle between upper and lower portions of the wavefront near its edges is less than 0.7° . The lower portion of the wavefront exhibits large and non-uniform losses of the signal. This artifact arises due to interference from a positive pressure wave possibly reflected from the sample support assembly. This interfering profile visible on Fig. 8b has an approximately cylindrical shape. The negative pressure wavefront (Fig. 8a) is followed by a significantly smaller and broadened positive wavefront (Fig. 8b) delayed by $\sim 60 - 130$ ns. This delayed signal is likely the result of reflection from the steel surface of a forward traveling positive pressure wave.

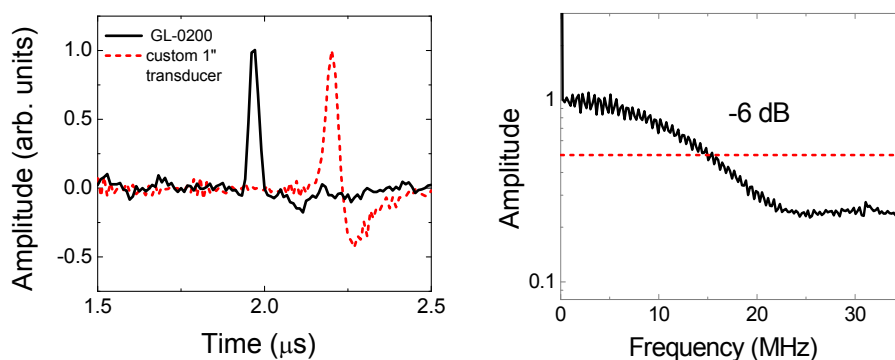


Figure 9. Impulse response from a single point of a planar wavefront and its corresponding frequency spectrum. The impulse response from the large transducer is shown as a dashed line for comparison.

The recorded flat wavefront indicates that the parabolic mirror performs spherical to plane wave conversion as expected and that the source emits a high-quality spherical wavefront. The impulse response of a small-size broadband GL-0200 transducer allows us to measure the frequency profile of the emitted spherical wave (Fig. 9). The corresponding FWHM and bandwidth of this pressure profile are ~ 34 ns and ~ 15 MHz, respectively. It is instructive to compare the measured pressure profiles of “small” and the “large” transducers in response to the same source of spherical waves. For the large detector, the peak time width of ~ 44 ns does not appear significantly larger, considering the dimensions of the transducer. However, there are strong indications that the observed narrow peak is not real and is the result of imperfect transducer alignment. Indeed, slightly misaligned (or slightly non-flat) transducer with large area will differentiate the incoming signals of the opposite signs. One may expect that the later portion of a broad impulse response from Fig. 4 will be canceled by a pressure wave of an opposite sign. The net result will appear as an overall reduction in pulse duration. These effects make transducer alignment extremely challenging, given that pulse duration is one the major indicators that guides the alignment process.

5. CONCLUSIONS

In this work, we have described and tested a novel application of an old idea: using an off-axis parabolic reflector for optoacoustic microscopy imaging. The offered design has a number of advantages over scanning optoacoustic microscopy systems. Unlike refractive elements, the parabolic surface made of high acoustic impedance materials will work as an ideal reflector that converts 100% of incoming spherical wavefront to a planar wave in a wide range of apertures. This conversion allows the use of readily available flat-surface transducers with any bandwidth for high-resolution imaging. Large collection efficiency of the system will improve its sensitivity and will allow the use of lower

frequencies to achieve the desired imaging resolution. This experimental setup has demonstrated the resolution of ~ 0.3 mm that matches the estimated theoretical limit defined by its current numerical aperture and the frequency bandwidth. Further improvements in terms of detector bandwidth and sensitivity, as well as system alignment procedures are underway. With these improvements, high-resolution optoacoustic imaging system based on off-axis parabolic reflector will become a viable alternative to available scanning optoacoustic microscopy designs.

REFERENCES

- [1] Oraevsky, A.A., Jacques, S.L., Esenaliev, R.O., Tittel, F.K., "Time-Resolved Optoacoustic Imaging in Layered Biological Tissues", in *Advances in Optical Imaging and Photon Migration*, Academic Press, p. 161-165 (1994).
- [2] Oraevsky, A.A., Karabutov, A.A., "Optoacoustic Tomography" in *Biomedical Photonics Handbook*, CRC Press, p. 34-1-4 (2003).
- [3] Xu M.H., Wang L.H.V., "Photoacoustic imaging in biomedicine", *Review of Scientific Instruments* 77(4), 041101-1-6 (2006).
- [4] Savateeva E.V., Karabutov A.A., Bell B., Johnigan R., Motamedi M., Oraevsky A.A., "Non-invasive detection and staging of oral cancer in vivo with confocal optoacoustic tomography (COAT)", *SPIE Proceedings* 3916, 55-66 (2000).
- [5] Maslov K., Stoica G., Wang L.H.V., "In vivo dark-field reflection-mode photoacoustic microscopy", *Optics Letters* 30(6), 625-627 (2005).
- [6] Zhang H.F., Maslov K., Wang L.H.V., "In vivo imaging of subcutaneous structures using functional photoacoustic microscopy", *Nature Protocols* 2(4), 797-804 (2007).
- [7] Zhang E., Laufer J., Beard P., "Backward-mode multiwavelength photoacoustic scanner using a planar Fabry-Perot polymer film ultrasound sensor for high-resolution three-dimensional imaging of biological tissues", *Applied Optics* 47(4), 561-577 (2008).
- [8] Laufer J., Zhang E., Raivich G., Beard P., "Three-dimensional noninvasive imaging of the vasculature in the mouse brain using a high resolution photoacoustic scanner", *Applied Optics* 48(10), D299-D306 (2009).
- [9] De La Zerda A., Liu Z.A., Bodapati S., Teed R., Vaithilingam S., Khuri-Yakub B.T., Chen X.Y., Dai H.J., Gambhir S.S., "Ultrahigh sensitivity carbon nanotube agents for photoacoustic molecular imaging in living mice", *Nano Letters* 10(6), 2168-2172 (2010).
- [10] Song K.H., Wang L.V., "Deep reflection-mode photoacoustic imaging of biological tissue", *Journal of Biomedical Optics* 12(6), 060503-1-3 (2007).
- [11] Fronheiser M.P., Stein A., Herzog D., Thompson S., Liopo A., Eghtedari M., Motamedi M., Ermilov S., Conjusteau A., Gharieb R., Lacewell R., Miller T., Mehta K., Oraevsky A.A., "Optoacoustic System for 3D Functional and Molecular Imaging in Nude Mice", *SPIE Proceedings* 6856, R0-R7 (2008).
- [12] Zhang H.F., Maslov K., Stoica G., Wang L.H.V., "Functional photoacoustic microscopy for high-resolution and noninvasive in vivo imaging", *Nature Biotechnology* 24(7), 848-51 (2006).
- [13] Maslov K.I., Dorozhkin L.M., Doroshenko V.S., Maev R.G., "A new focusing ultrasonic transducer and two foci acoustic lens for acoustic microscopy", *IEEE Transactions on Ultrasonics Ferroelectrics and Frequency Control* 44(2), 380-385 (1997).
- [14] Zhang E.Z., Laufer J.G., Pedley R.B., Beard P.C., "In vivo high-resolution 3D photoacoustic imaging of superficial vascular anatomy", *Physics in Medicine and Biology* 54(4), 1035-1046 (2009).
- [15] Onda, "Tables of Acoustic Properties of Materials. http://www.ondacorp.com/tecref_acoustictable.shtml"
- [16] Kino, G.S., [Acoustic Waves: Devices, Imaging, and Analog Signal Processing], Prentice-Hall; (1987).
- [17] Goss S.A., Johnston R.L., Dunn F. "Comprehensive Compilation of Empirical Ultrasonic Properties of Mammalian-Tissues", *Journal of the Acoustical Society of America* 64(2), 423-57 (1978).
- [18] Duck, F.A., [Physical Properties of Tissues: a Comprehensive Reference Handbook], (1990).
- [19] Conjusteau A., Ermilov S.A., Su R., Brecht H.P., Fronheiser M.P., Oraevsky A.A., "Measurement of the spectral directivity of optoacoustic and ultrasonic transducers with a laser ultrasonic source", *Review of Scientific Instruments* 80(9), 093608-1-6 (2009).